mathematics

MDPI

Article

Nonlinear Bending of Sandwich Plates with Graphene Nanoplatelets Reinforced Porous Composite Core under Various Loads and Boundary Conditions

Xudong Fan [1], Aiwen Wang [1,*], Pengcheng Jiang [1], Sijin Wu [2] and Ying Sun [1]

1 School of Applied Science, Beijing Information Science and Technology University, Beijing 100192, China
2 School of Instrument of Science and Opto Electronics Engineering, Beijing Information Science and Technology University, Beijing 100192, China
* Correspondence: wangaiwen@bistu.edu.cn

Abstract: The nonlinear bending of the sandwich plates with graphene nanoplatelets (GPLs) reinforced porous composite (GNRPC) core and two metal skins subjected to different boundary conditions and various loads, such as the concentrated load at the center, linear loads with different slopes passing through the center, linear eccentric loads, uniform loads, and trapezoidal loads, has been presented. The popular four-unknown refined theory accounting for the thickness stretching effects has been employed to model the mechanics of the sandwich plates. The governing equations have been derived from the nonlinear Von Karman strain–displacement relationship and principle of virtual work with subsequent solution by employing the classical finite element method in combination with the Newton downhill method. The convergence of the numerical results has been checked. The accuracy and efficiency of the theory have been confirmed by comparing the obtained results with those available in the literature. Furthermore, a parametric study has been carried out to analyze the effects of load type, boundary conditions, porosity coefficient, GPLs weight fraction, GPLs geometry, and concentrated load radius on the nonlinear central bending deflections of the sandwich plates. In addition, the numerical results reveal that the adopted higher order theory can significantly improve the simulation of the transverse deflection in the thickness direction.

Keywords: nonlinear bending; graphene nanoplatelets reinforced porous sandwich plates; various loads; four-unknown refined theory

MSC: 74H45

Citation: Fan, X.; Wang, A.; Jiang, P.; Wu, S.; Sun, Y. Nonlinear Bending of Sandwich Plates with Graphene Nanoplatelets Reinforced Porous Composite Core under Various Loads and Boundary Conditions. *Mathematics* **2022**, *10*, 3396. https://doi.org/10.3390/math10183396

Academic Editor: Fernando Simoes

Received: 6 August 2022
Accepted: 14 September 2022
Published: 19 September 2022

1. Introduction

Metal foam core sandwich structures have received considerable attention due to the advantages of lightweight, energy dissipation capacity, etc. [1,2]. However, the existence of pores resulting in the relative reduction of stiffness limits its application in the case of heavy load bearing [3]. A large number of theoretical and experimental studies [4–8] show that a small addition of GPLs to the matrix can significantly improve the mechanical properties of the structure. Therefore, GPLs as reinforcement has been developed by some researchers to the sandwich structures with porous core. By this way, not only can the stiffness be enhanced without increasing the weight, but the required mechanical properties can be obtained by altering the size and density of the internal pores in different directions as well as the weight fraction and distribution pattern of GPLs [9,10]. Therefore, the sandwich plates with GPLs reinforced porous composite (GNRPC) cores exhibit the high potential of use as one or more components of the aerospace structures.

Significant efforts have been devoted to study the mechanical behavior of the sandwich structures with porous core. The studies are mainly divided into two categories. For the sandwich structures with nanofiller (carbon nanotubes, GPLs, etc.) reinforced composite face sheets, Yu [11] dealt with the buckling and postbuckling behavior of a sandwich plate with a homogeneous core resting on an elastic foundation in thermal environments based on Reddy's high order shear deformation plate theory (HSDT). Allam [12] presented hygrothermal stress analysis of rotating functionally graded (FG) graphene/metal sandwich cylindrical shell with an auxetic honeycomb core using the first-order shear deformation theory (FSDT). Arefi [13] studied buckling and free vibration analyses of sandwich beam made of a softcore using the Ritz method and extended higher-order sandwich panel theory. Nguyen [14] proposed an excellent computational approach based on polygonal meshes to comprehensively examine the free vibration, buckling, and dynamic instability behaviors of the auxetic honeycomb sandwich plate structure using the generalized C^0–HSDT [15]. Li [16] investigated multiscale modeling and nonlinear low-velocity impact analysis of sandwich plates with FG auxetic 3D lattice cores based on FSDT. Yadav [17] considered the nonlinear static analysis of circular cylindrical sandwich shells using a HSDT with nine kinematic parameters. On the basis of Reddy's HSDT, all the following studies were conducted. Karimiasl [18] analyzed the nonlinear free and forced vibration analysis of composite sandwich panel subjected to the harmonic force excitation in the hygrothermal environment. Safaei [19] explored the thermal and mechanical buckling behaviors of lightweight polymeric nanocomposite sandwich plates containing uniformly dispersed pores resting on two-parameter elastic foundations based. For the structures with GNRPC core, Tao [20] discussed the postbuckling behavior of sandwich cylindrical shell panels subjected to central point loads and uniform and nonuniform pressure loadings. Yaghoobi [3] provided a robust and accurate analytical solution for establishing the buckling capacity of a series of simply supported sandwich plates. Chen performed modeling and analysis of compressive and thermal postbuckling of sandwich cylindrical panels supported by an elastic foundation [21] and surrounded by an elastic medium [22]. Twinkle [23] employed a semianalytical approach to obtain the buckling and free vibration characteristics of sandwich cylindrical panel. Li [24] examined the nonlinear vibration and the dynamic buckling of sandwich plates thoroughly. A few studies have been devoted to the structures with porous face layers. For instance, based on the framework of the FSDT, nonlinear large amplitude vibration analysis of the conical sandwich panels with porous piezoelectric face layers resting on the nonlinear elastic foundation has been conducted by Zhu [25].

From the above review, based on the available deformation theories, many mechanical studies have been carried out for the nanofiller reinforced sandwich structures. As we know, the accurate and high efficient displacement field is crucial for researchers to accurately predict the mechanical behavior of composite sandwich structures. Generally, the core layer thickness of the sandwich structure is much longer than the surface layer in engineering applications. It is straightforward to cause the transverse stretching or compressive deformation for thick structures. However, the displacement field employed in the above literature studies ignored the transverse tensile effect, thus leading to inaccuracy in the calculations.

In the currently available literature, the bending and elastic stability analyses considering the thickness stretch effect in the GNRPC curved beams [26] have been performed. However, to the best of the author's knowledge, there are few studies in the open literature on the mechanical behavior of the GNRPC sandwich plates taking the stretching effect into account. Furthermore, the research on the nonlinear bending behavior under different loads and different boundary conditions is even less.

In this study, the author's aim is to carry out the nonlinear bending of the sandwich plates with a GNRPC core and two metal skins under various loads in combination with different boundary conditions based on the four variable shear deformation theory [27] accounting for the stretching effects. The kinetic equation of the sandwich plates has been derived from the principle of virtual work. The nonlinear system was solved by employing the finite element [28,29] and Newton downhill [29,30] methods. The convergence and the validation of the numerical method has been verified by comparing the transverse bending deflection with that of the available published literature. In addition, the effects of various physical and geometrical parameters on the dimensionless central transverse bending deflection for the porous sandwich plates have been analyzed.

2. Characteristic Material Parameters

A sandwich porous plate with length a, width b, two skin layers with thickness h_f, and core layer with thickness h_c has been depicted in Figure 1. The skin layers are made of metal, whereas the porous core layer is composed of N_L layers of the GPLs reinforced composite [30], with its cross-section shown in Figures 2 and 3.

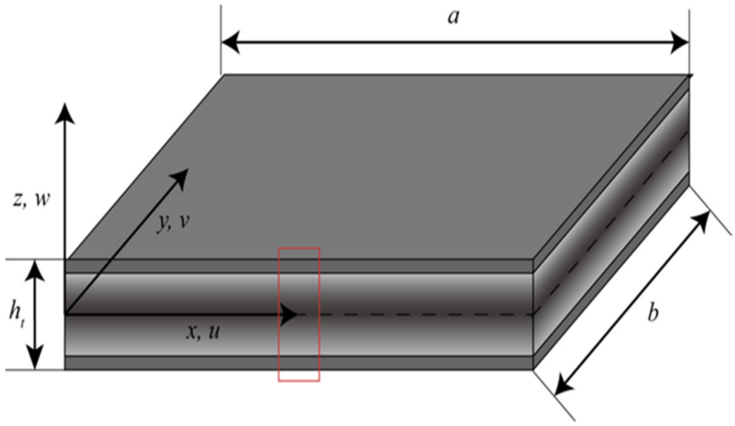

Figure 1. The geometry of the sandwich plate with GPLs reinforced porous core layer.

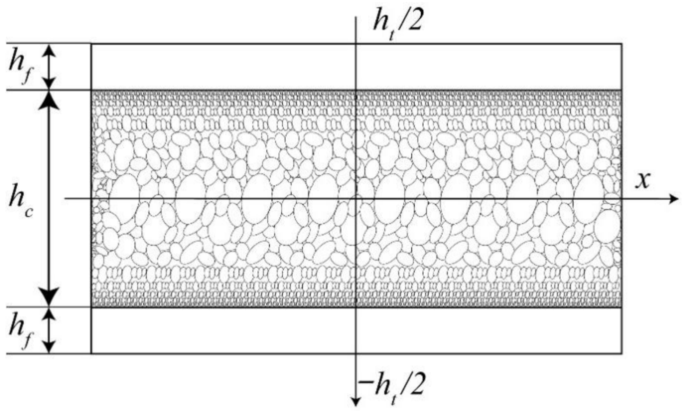

Figure 2. The cross-section of the porous core layer.

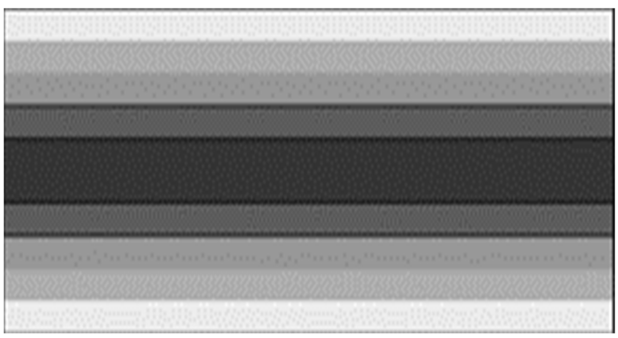

Figure 3. The cross-section of GPLs reinforced core layer.

The GPL volume fraction of the ith layer can be calculated by

$$V_G^{(i)} = \frac{f_G^{(i)}}{f_G^{(i)} + (\rho_G/\rho_M)(1 - f_G^{(i)})}. \tag{1}$$

where, $f_G^{(i)}$ is the GPL weight fraction of the ith core layer of the sandwich plate, as follows [30]:

$$f_G^{(i)} = 4f_G\left(\frac{N_L+1}{2} - \left|i - \frac{N_L+1}{2}\right|\right)/(2+N_L).i = 1,2,\ldots,N_L \tag{2}$$

and f_G is total GPL weight fraction.

The subscripts "G" and "M" denote GPLs and matrix, respectively. "E", "ρ", and "μ" represent Young's modulus, mass density, and Poisson's ratio respectively. The common approach adopted to estimate the effective Young's modulus of the individual core layer without porosity is the modified Halpin–Tsai model [5–8] as follows:

$$E^* = \frac{3}{8}\frac{1+\xi_L\eta_L V_G^{(i)}}{1-\eta_L V_G^{(i)}} \times E_M + \frac{5}{8}\frac{1+\xi_W\eta_W V_G^{(i)}}{1-\eta_W V_G^{(i)}} \times E_M. \tag{3}$$

where,

$$\eta_L = \frac{(E_G/E_M)-1}{(E_G/E_M)+\xi_L}, \eta_W = \frac{(E_G/E_M)-1}{(E_G/E_M)+\xi_W}, \xi_L = \frac{2l_G}{h_G}, \xi_W = \frac{2w_G}{h_G}. \tag{4}$$

l_G, w_G, and h_G represent the average length, width and thickness of the GPLs, respectively. Poisson's ratio $\mu*$ can be expressed by the following rule of mixtures [5–8]:

$$\mu* = \mu_G V_G^{(i)} + \mu_M\left(1 - V_G^{(i)}\right). \tag{5}$$

Furthermore, Young's modulus $E(z)$ and Poisson's ratio $\mu(z)$ of the porous core layer can be denoted as follows [24]:

$$E(z) = E^*[1 - e_0\lambda(z)]. \tag{6}$$

$$\mu(z) = \mu*. \tag{7}$$

where, the nonuniform symmetric porosity distribution can be described as [24]:

$$\lambda(z) = \cos\left(\frac{\pi z}{h_c}\right). \tag{8}$$

The porosity coefficient is $e_0 = 1 - \frac{E_2}{E_1}$, where E_2, E_1 are the maximum and minimum Young's modulus, respectively.

3. Theoretical Formulation

The following four variable shear deformation theory [27] considering the stretching effects is assumed:

$$\begin{aligned} u_1(x,y,z) &= u(x,y) - z\tfrac{\partial w}{\partial x} + f(z)\tfrac{\partial \varphi}{\partial x}, \\ u_2(x,y,z) &= v(x,y) - z\tfrac{\partial w}{\partial y} + f(z)\tfrac{\partial \varphi}{\partial y}, \\ u_3(x,y,z) &= w(x,y) + g(z)\varphi(x,y). \end{aligned} \tag{9}$$

A nonlinear strain–displacement relation can be presented as follows:

$$\begin{aligned} &\varepsilon_{xx} = u_{1,x} + \tfrac{1}{2}(u_{3,x})^2, \varepsilon_{yy} = u_{2,y} + \tfrac{1}{2}(u_{3,y})^2, \varepsilon_{zz} = u_{3,z} + \tfrac{1}{2}(u_{3,z})^2, \\ &\gamma_{xy} = u_{1,y} + u_{2,x} + u_{3,x}u_{3,y}, \gamma_{xz} = u_{1,z} + u_{3,x}, \gamma_{yz} = u_{2,z} + u_{3,y}. \end{aligned} \tag{10}$$

where the subscripts '$,x$' and '$,y$' represent the partial derivatives with respect to x and y directions. Let

$$\boldsymbol{\varepsilon}^{\boldsymbol{T}} = (\varepsilon_{xx}, \varepsilon_{yy}, \varepsilon_{zz}, \gamma_{xy}, \gamma_{xz}, \gamma_{yz}),$$

$$\boldsymbol{q}^{\boldsymbol{T}} = (u_{,x}, u_{,y}, v_{,x}, v_{,y}, w_{,x}, w_{,y}, w_{,xx}, w_{,xy}, w_{,yy}, \varphi, \varphi_{,x}, \varphi_{,y}, \varphi_{,xx}, \varphi_{,xy}, \varphi_{,yy}).$$

Here, the superscript $\boldsymbol{T}$ represents the transposed operator. The strain vector $\boldsymbol{\varepsilon}$ can be written in the following matrix form:

$$\boldsymbol{\varepsilon} = \boldsymbol{Z}\left[\boldsymbol{H} + \frac{1}{2}\boldsymbol{A}(\boldsymbol{q})\right]\boldsymbol{q}, \tag{11}$$

The detailed forms of $\boldsymbol{H}$ and $\boldsymbol{A}$ have been listed in the Appendix A. The relation between stress $\boldsymbol{\sigma}^{(k)} = (\sigma_{xx}^{(k)}, \sigma_{yy}^{(k)}, \sigma_{zz}^{(k)}, \tau_{xy}^{(k)}, \tau_{xz}^{(k)}, \tau_{yz}^{(k)})^T$ and strain at layer $\boldsymbol{k}$ in the sandwich plate can be assumed as follows:

$$\boldsymbol{\sigma}^{(k)} = \boldsymbol{Q}^{(k)}\boldsymbol{\varepsilon}. \tag{12}$$

$$\boldsymbol{Q}^{(k)} = \begin{bmatrix} Q_{11}^{(k)} & Q_{12}^{(k)} & Q_{13}^{(k)} & & & \\ Q_{21}^{(k)} & Q_{22}^{(k)} & Q_{23}^{(k)} & & & \\ Q_{31}^{(k)} & Q_{32}^{(k)} & Q_{33}^{(k)} & & & \\ & & & Q_{44}^{(k)} & & \\ & & & & Q_{55}^{(k)} & \\ & & & & & Q_{66}^{(k)} \end{bmatrix} \tag{13}$$

$$Q_{11}^{(k)} = Q_{22}^{(k)} = Q_{33}^{(k)} = \frac{E^{(k)}(z)(1 - v^{(k)})}{(1 - 2v^{(k)})(1 + v^{(k)})},$$

$$Q_{12}^{(k)} = Q_{13}^{(k)} = Q_{23}^{(k)} = \frac{E^{(k)}(z)v^{(k)}}{(1 - 2v^{(k)})(1 + v^{(k)})},$$

$$Q_{44}^{(k)} = Q_{55}^{(k)} = Q_{66}^{(k)} = \frac{E^{(k)}(z)}{2(1 + v^{(k)})}.$$

Supposing $k = 1$ and $k = N_L + 2$ denote the upper and lower surfaces, and k = $2, \cdots, N_L + 1$ represents the core layer. Correspondingly, Young's modulus $E^{(k)}(z)$ and Poisson's ratio $\nu^{(k)}(z)$ can be computed as follows:

$$E^{(k)}(z) = \begin{cases} E_M, & k = 1, N_L + 2 \\ E^*, & k = 2, \cdots, N_L + 1 \end{cases} \tag{14}$$

$$\nu^{(k)}(z) = \begin{cases} \mu_M, & k = 1, N_L + 2 \\ \mu^*, & k = 2, \cdots, N_L + 1 \end{cases} \tag{15}$$

Based on (11), the stress resultant vector in the thickness direction can be written as:

$$S = D\left[H + \frac{1}{2}A(q)\right]q. \tag{16}$$

The internal virtual work is represented as:

$$\delta P_{\text{int}} = \sum_{k=1}^{N} \iint_A \int_{z_k}^{z_{k+1}} \delta\varepsilon^T \sigma^{(k)} dz dx dy = \iint_A \delta q^T \left[H^T + \frac{1}{2}A^T(\delta q_s)\right] S dx dy \tag{17}$$

On the other hand, the external virtual work is:

$$\delta P_{ext} = \iint_A \delta q^T p dx dy \tag{18}$$

where, p is the external force acting on the surface of the sandwich plate.

The weak form of the nonlinear governing equations can be written as:

$$\iint_A \delta q^T \left\{ \left[H^T + \frac{1}{2}A^T(\delta q)\right] S - p \right\} dx dy = 0. \tag{19}$$

$$\begin{pmatrix} N \\ M \\ P \\ R \\ S \\ L \end{pmatrix} = \begin{pmatrix} N_{xx} & N_{yy} & N_{zz} & N_{xy} & N_{xz} & N_{yz} \\ M_{xx} & M_{yy} & M_{zz} & M_{xy} & M_{xz} & M_{yz} \\ P_{xx} & P_{yy} & P_{zz} & P_{xy} & P_{xz} & P_{yz} \\ R_{xx} & R_{yy} & R_{zz} & R_{xy} & R_{xz} & R_{yz} \\ S_{xx} & S_{yy} & S_{zz} & S_{xy} & S_{xz} & S_{yz} \\ L_{xx} & L_{yy} & L_{zz} & L_{xy} & L_{xz} & L_{yz} \end{pmatrix} = \sum_{k=1}^{N} \int_{z_k}^{z_{k+1}} \sigma^{(k)} \begin{pmatrix} 1 \\ z \\ g(z) \\ g^2(z) \\ f(z) \\ f'(z) + g(z) \end{pmatrix} dz. \tag{20}$$

4. Finite Element Discretization

The nonlinear system in Equation (19) has been solved by employing the finite element method [28,29]. The midplane displacements u, v are interpolated by the 4-node Lagrange bilinear shape functions $\phi = \{\phi_i\}, i = 1, 2, 3, 4$, as

$$u = \phi u^e,\ v = \phi v^e \phi_i(\xi, \eta) = \frac{1}{4}(1 + \xi\xi_i)(1 + \eta\eta_i). \tag{21}$$

in natural coordinates $(\xi, \eta) \in [-1, 1] \times [-1, 1]$. The interpolation of the other displacements w, φ and their derivatives is dependent on the 4-nodes nonconforming rectangular functions as

$$w = N_H w^e,\ \varphi = N_H \varphi^e. \tag{22}$$

where, the interpolating functions N_H [31,32] are as follows:

$$\begin{aligned} N_H &= \{H_1, H_{1x}, H_{1y}, H_2, H_{2x}, H_{2y}, \cdots, H_4, H_{4x}, H_{4y}\} \\ H_i &= \tfrac{1}{8}(1 + \xi_i\xi)(1 + \eta_i\eta)\left(2 + \xi_i\xi + \eta_i\eta - \xi^2 - \eta^2\right), \\ H_{ix} &= \tfrac{le}{8}\xi_i(\xi_i\xi - 1)(1 + \eta_i\eta)(1 + \xi_i\xi)^2,\ \ i = 1, 2, 3, 4. \\ H_{iy} &= \tfrac{le}{8}\eta_i(\eta_i\eta - 1)(1 + \xi_i\xi)(1 + \eta_i\eta)^2, \end{aligned} \tag{23}$$

where, $\xi_i,\ \eta_i$ in Equations (21) and (23) are the corresponding nodal coordinates in the natural reference system.

Based on the interpolation, the discretized unknowns can be written as:

$$q = G\theta^e. \tag{24}$$

where, G is an interpolating matrix constructed by the components of the interpolating functions N_H and their derivative with respect to the local coordinates ξ, η. The unknown vector can be written as $\theta^{eT} = \{\theta_1^e, \theta_2^e, \theta_3^e, \theta_4^e\}$ where,

$$\theta_i^{eT} = \{u_{i,x}, v_{i,x}, v_{i,y}, w_{i,x}, w_{i,y}, w_{i,xx}, w_{i,xy}, w_{i,yy},\ \varphi_i, \varphi_{i,x}, \varphi_{i,y}, \varphi_{i,xx}, \varphi_{i,xy}, \varphi_{i,yy}\}^e$$

By substituting Equations (21)–(23) into (19), the finite element discrete scheme of Equation (19) at the elemental level is gained as follows:

$$\begin{cases} \delta\theta^{eT} \iint_A G^T \left\{ \left[H^T + \tfrac{1}{2} A^T(\delta\theta^e) \right] S^e - p \right\} dxdy = 0. \\ S^e = D\left[H + \tfrac{1}{2} A(\theta^e) \right] G\theta^e. \end{cases} \tag{25}$$

According to the classical finite element method [28], a global stiffness matrix and a nonlinear system for the sandwich plate are formed. Then, the Newton downhill method [29,30] is subsequently applied to solve the nonlinear system.

5. Numerical Results and Analysis

In order to reveal the nonlinear bending mechanical behavior of the sandwich plates with GNRPC core and two aluminum skins under various loads, the following loads are considered in this study: uniform load (UL), concentrated load (CL) with radius CR around the center $\left(\frac{a}{2}, \frac{b}{2}, \frac{h}{2}\right)$, linear eccentric load (EL), linear loads with infinite slope (LL_∞), and slope k (LL_k) passing through the center and trapezoidal load (TL), as shown in Figure 4.

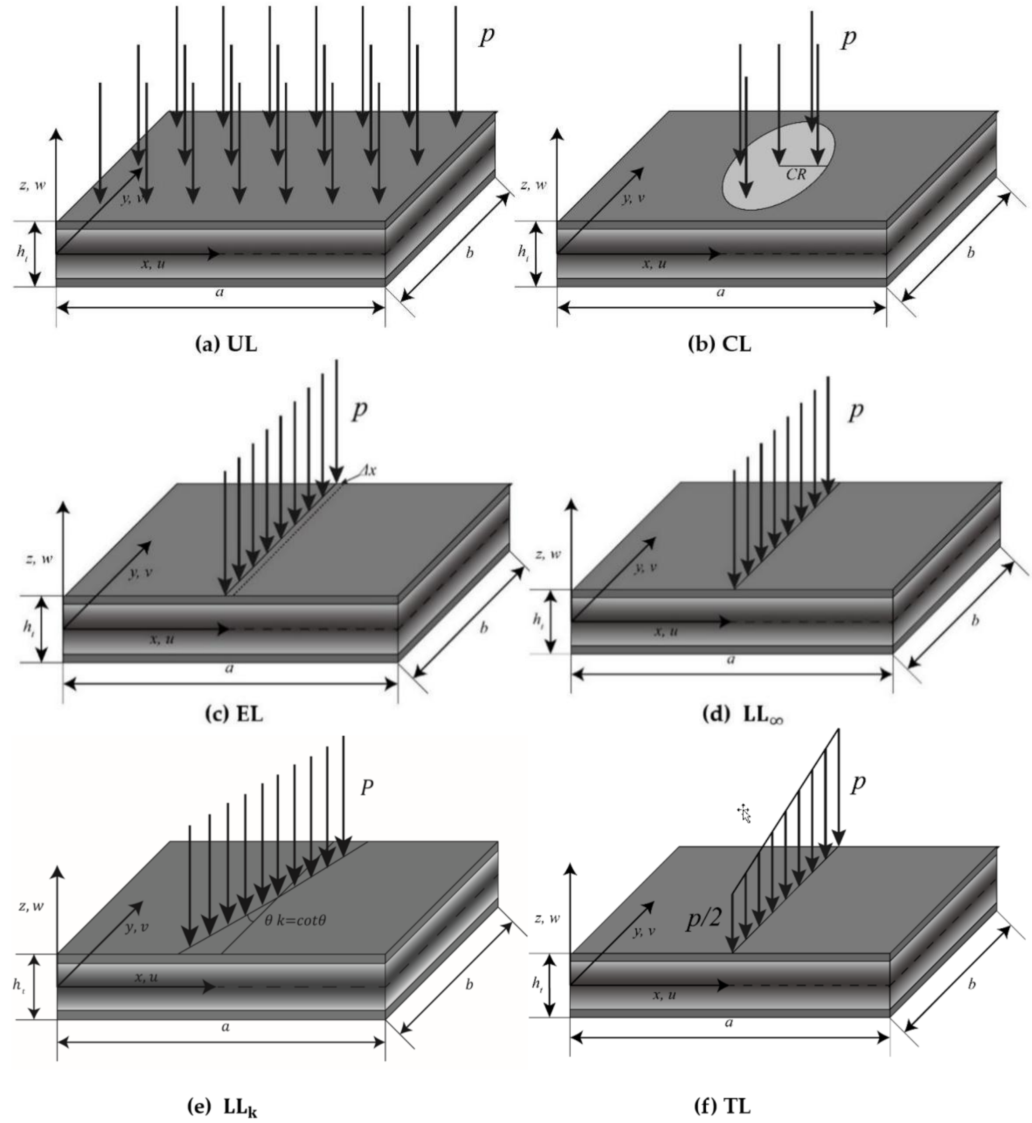

Figure 4. The type of loads: (**a**) uniform load, (**b**) concentrated load, (**c**) eccentric load, (**d**) linear loads with infinite slope, (**e**) linear loads with slope k, (**f**) trapezoidal load.

5.1. Parameters and Validation

Aluminum was taken as matrix, and GPLs were used as reinforcement. The material parameters have been listed in Table 1 [24].

Table 1. Material parameters of GPLs and aluminum.

Material	Young's Modulus	Poisson's Ratio	Density
Al	$E_1 = 70$ Gpa	$v_1 = 0.3$	$\rho_1 = 2702\ \mathrm{kg/m^3}$
(CrO_2)-1	$E_2 = 200$ Gpa	$v_2 = 0.3$	$\rho_2 = 5700\ \mathrm{kg/m^3}$

Unless otherwise stated, the other parameters are as follows:

$$a = 1\mathrm{m}, h_t = 0.005\mathrm{a}, h_f = 0.1\mathrm{h}_t, h_c = 0.8\mathrm{h}_t, e_0 = 0.5, CR = 0.1\mathrm{m}$$

$$l_G = 2.5\mu\mathrm{m}, w_G = 1.5\mu\mathrm{m}, h_G = 1.5\mathrm{nm}, W_G = 0.5\%.$$

In order to clearly represent the boundary conditions, the following symbolic assumptions have been made.

Simply supported (S):

$$v = w = w_{,y} = \varphi = \varphi_{,y} = M_{xx} = S_{xx} = 0 \text{ at } x = 0, a. \tag{26}$$

$$u = w = w_{,x} = \varphi = \varphi_{,x} = M_{xx} = S_{xx} = 0 \text{ at } y = 0, b. \tag{27}$$

Clamped (C):

$$u = w = w_{,x} = \varphi = \varphi_{,x} = M_{yy} = S_{yy} = 0 \text{ at } x = 0, a, \ y = 0, b. \tag{28}$$

Based in this notation, the classical boundary conditions can be represented by a combination of four letters, such as CCCC, SSSS, SCSC, CFCF, etc. In the following numerical experiment, the initials represent the boundary of the edge at $y = 0$, followed by the combination in a counter clockwise order. Thus, the last letter denotes the side $x = 0$, as shown in Figure 5.

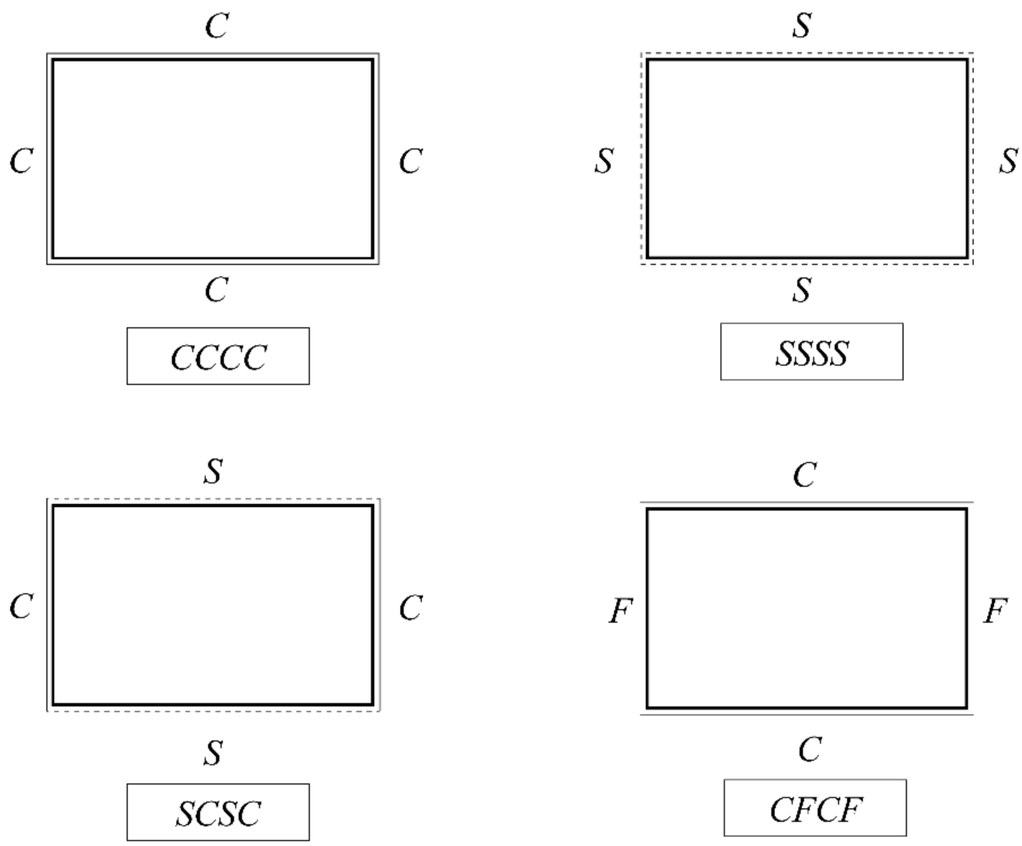

Figure 5. Schematic diagram of the boundary conditions.

First, two case study are performed to verify the convergence of the present numerical model. One is for nonlinear bending of the aluminum/alumina (Al/ZrO2-1) functionally graded materials (FGM) square plate under SSSS boundary condition and uniform load. The equivalent material properties with gradient change in the thickness direction are expressed by $P(z)$.

$$P(z) = P_1 + (P_2 - P_1)V(z) \tag{29}$$

$$V(z) = \left(\frac{1}{2} + \frac{z}{h}\right)^{v}. \tag{30}$$

where, $V(z)$ is the volume fraction of ZrO_2-1 with index v. P_1 and P_2 indicate the properties of Al and ZrO_2-1, respectively. The values of the material parameters and detailed computing methodology can be found in Ref. [33]. The other is for the nonlinear bending of sandwich plates with GNRPC core under four different boundary conditions (CCCC, SSSS, SCSC, CFCF) and three length-to-thickness ratios ($a/h_t = 20, 40, 60$). The dimensionless central deflections of FGM square plates and sandwich plates with GNRPC core are shown in Table 2 and Figure 6. Convergence behavior of dimensionless central deflection under different boundary conditions, respectively. It is clearly observed from Table 2. and Figure 6 that the dimensionless central deflections are converging well with the mesh refinement for different volume fraction index v of ZrO_2-1 and various boundary conditions as well as length-to-thickness ratios. Therefore, a 30×30 mesh is employed for the following numerical experiments.

Table 2. Convergence of dimensionless central deflection of FGM square plate.

Element Number	v			
	0	**0.5**	**1**	**2**
20×20	0.1752	0.2392	0.2834	0.3296
30×30	0.1750	0.2390	0.2830	0.3292
40×40	0.1749	0.2389	0.2829	0.3291
50×50	0.1749	0.2389	0.2828	0.3290
60×60	0.1749	0.2388	0.2828	0.3290

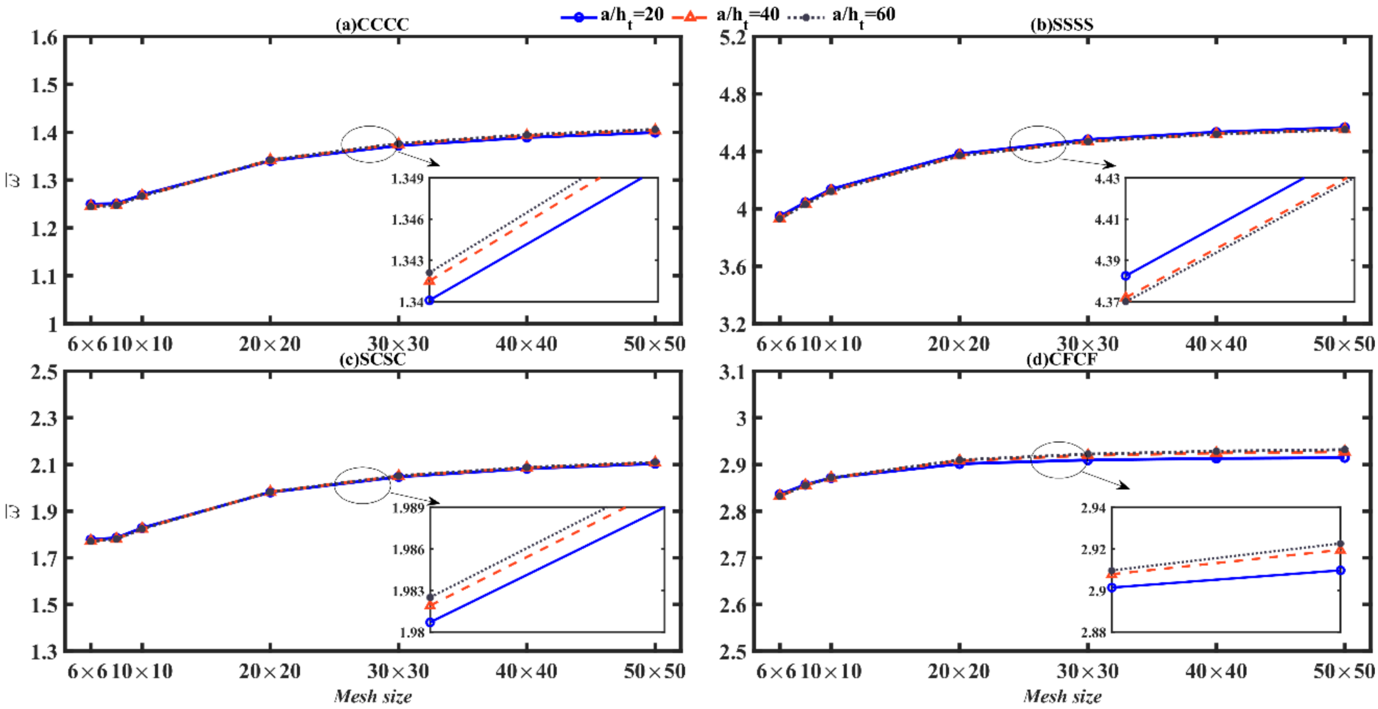

Figure 6. Convergence behavior of dimensionless central deflection under different boundary conditions.

Secondly, a further comparison study has been performed for the above FGM square plates. The dimensionless central deflections of FGM square plates under SSSS boundary conditions has been compared with those in open literature studies [33–36] and the simulation results by software ANSYS in Table 3. Table 4 considers the comparison of the dimensionless central deflection of FGM square plate under other three boundary conditions (CCCC, SCSC, SFSF). The coherence of the numerical results indicates the correctness and successful validation of the model and numerical calculation process depending on the finite element method.

Table 3. Comparison of dimensionless central deflection of FGM square plate.

Method	v			
	0	**0.5**	**1**	**2**
Present	0.1752	0.2392	0.2834	0.3296
Ref. [32]	0.1717	0.2319	0.2716	0.3121
Ref. [33]	0.1703	0.2232	0.2522	0.2827
Ref. [34]	0.1671	0.2505	0.2905	0.3280
Ref. [35]	0.1722	0.2403	0.2811	0.3221
Ansys	0.1541	0.2594	0.2793	0.3013

Table 4. Comparison of dimensionless central deflection of FGM square plate under three boundary conditions.

Boundary Conditions	**Method**	v			
		0	**0.5**	**1**	**2**
CCCC	Present	0.0692	0.0938	0.1113	0.1308
	Ref. [34]	0.0731	0.1073	0.1253	0.1444
	Ref. [35]	0.0773	0.1034	0.1207	0.1404
SCSC	Present	0.0941	0.1282	0.1522	0.1783
	Ref. [34]	0.1017	0.1501	0.1751	0.2008
	Ref. [35]	0.1073	0.1447	0.1701	0.1953
SFSF	Present	0.5177	0.6830	0.7795	0.8805
	Ref. [34]	0.5019	0.7543	0.8708	0.9744
	Ref. [35]	0.5061	0.7029	0.8214	0.9423

5.2. Nonlinear Bending Analysis of Sandwich Plates with GNRPC Core

The dimensionless central deflection at central point $\left(\frac{a}{2}, \frac{b}{2}, z\right)$ along the thickness of the sandwich plates under different loads and boundary conditions have been depicted in Figure 7. It is interesting to note that the dimensionless central deflection follows same behaviors for all six types of loads, which varies with z coordinate and exhibits the influence of the stretching effect in the thickness direction. According to the magnitude of dimensionless central deflections, the load types are sorted. For CCCC and CFCF boundary conditions, the order from large to small is UL, LL_{10}, CL with CR = 0.1 m, LL_∞, TL, EL. However, for SSSS and SCSC boundary conditions, CL and LL_∞ are fine tuned in the above sorting. The dimensionless central normal stress $\overline{\sigma}_{xx} = \frac{\sigma_{xx}(a/2,b/2,z)}{q_0 a^2/{h_t}^2}$, $q_0 = \frac{100pa^4}{E_m {h_t}^4}$ and shear stress $\overline{\tau_{yz}} = \frac{\tau_{yz}(a/2,0,z)}{q_0 a/h}$ have also been illustrated in Figures 8 and 9. It can be observed that all load types have the same nature. The normal stress in X-direction and shear stress are negative on the bottom surface and positive on the upper surface of the sandwich plates subjected to various loads and different boundary conditions. The transverse shear deformation distribution of all six loads is parabolic and fully satisfies the zero shear stress conditions on the surfaces.

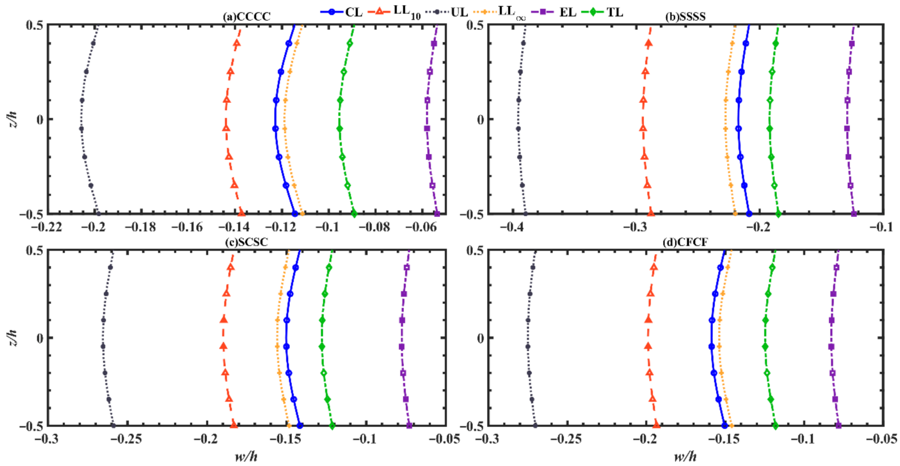

Figure 7. The dimensionless central deflection along the thickness direction.

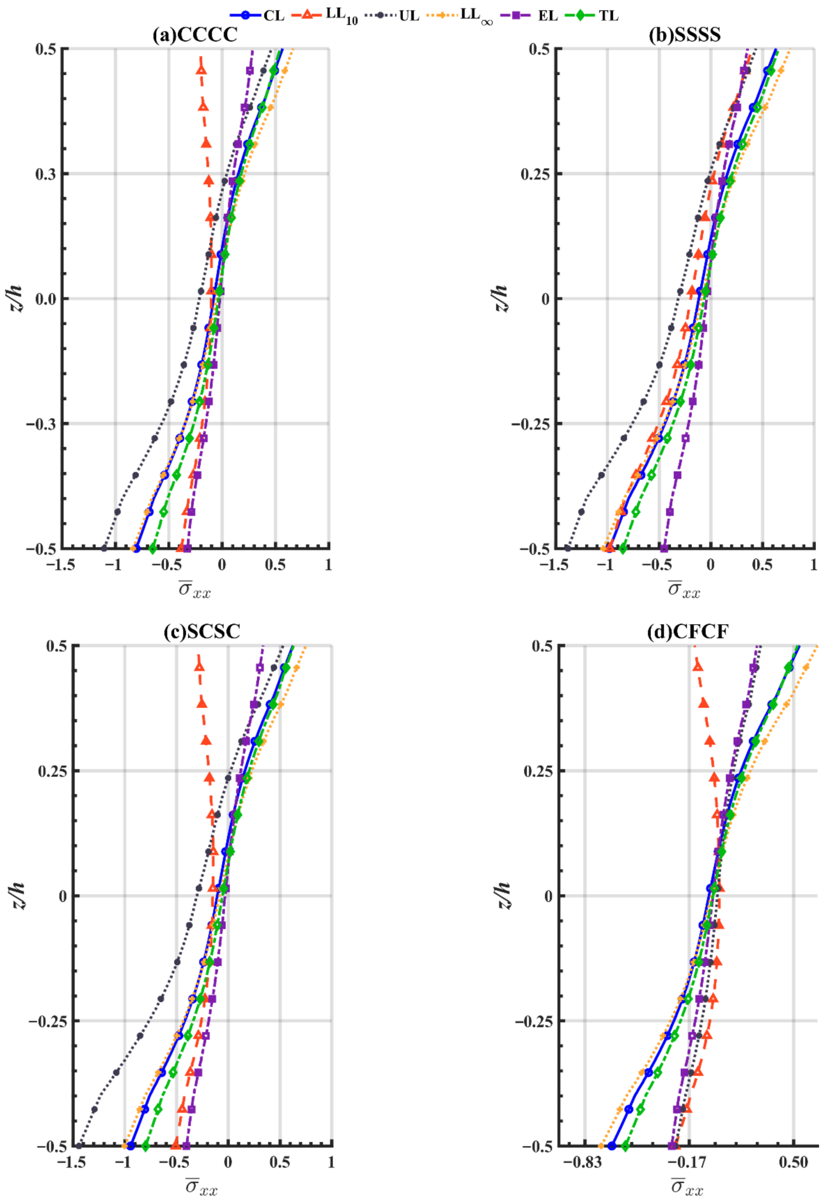

Figure 8. The dimensionless normal stress $\overline{\sigma}_{xx}\left(\frac{a}{2},\frac{b}{2},z\right)$ along the thickness direction.

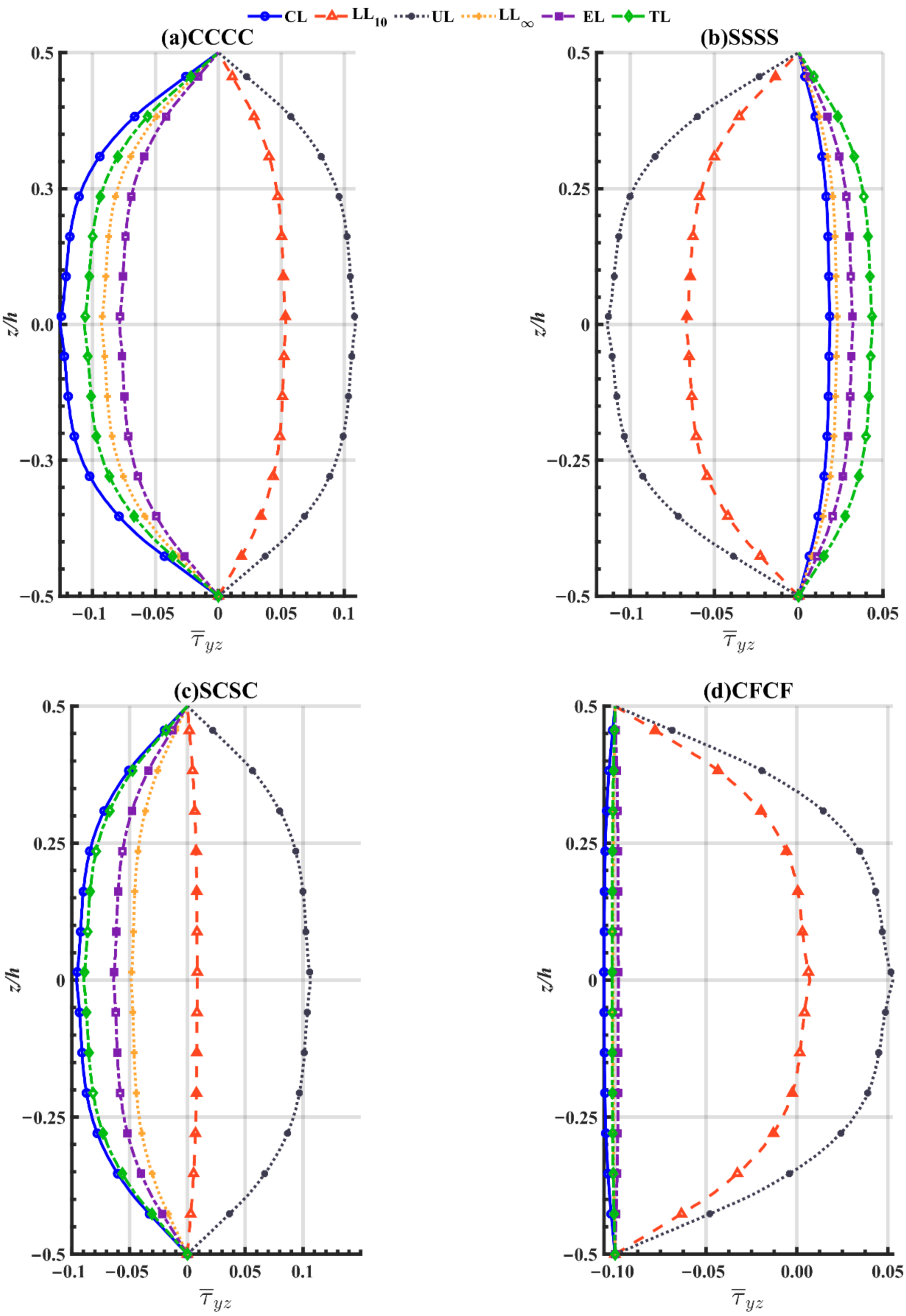

Figure 9. The dimensionless shear stress $\overline{\tau}_{yz}$ $(a/2, 0, z)$ along the thickness direction.

The central load-deflection curves of the sandwich plates subjected to the different loads and boundary conditions are depicted in Figure 10. It is observed that the dimensionless central bending deflection increases in a curve as all types of load increases. Besides, It can also be seen from Figures 7 and 10 that among all the type of loads, UL loads give the maximum dimensionless central deflection, EL load (0.5 cm off center) generates the minimum ones.

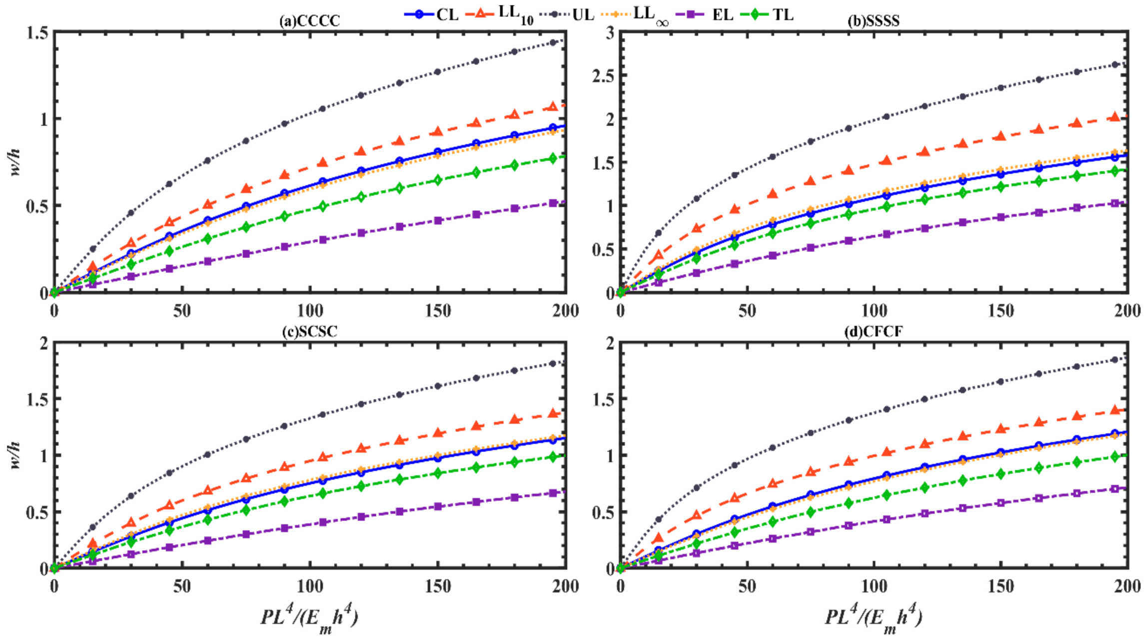

Figure 10. The central load-deflection curves of the sandwich plates subjected to various loads and boundary conditions.

The effect of porosity on the dimensionless central deflection of the sandwich plates has been presented in Figure 11. It is observed the dimensionless central deflection increase with an increment in porosity coefficient. This phenomenon is due to the fact that the existence of pores can significantly reduce the overall stiffness of the sandwich plates. Moreover, the larger porosity coefficient, the smaller the stiffness.

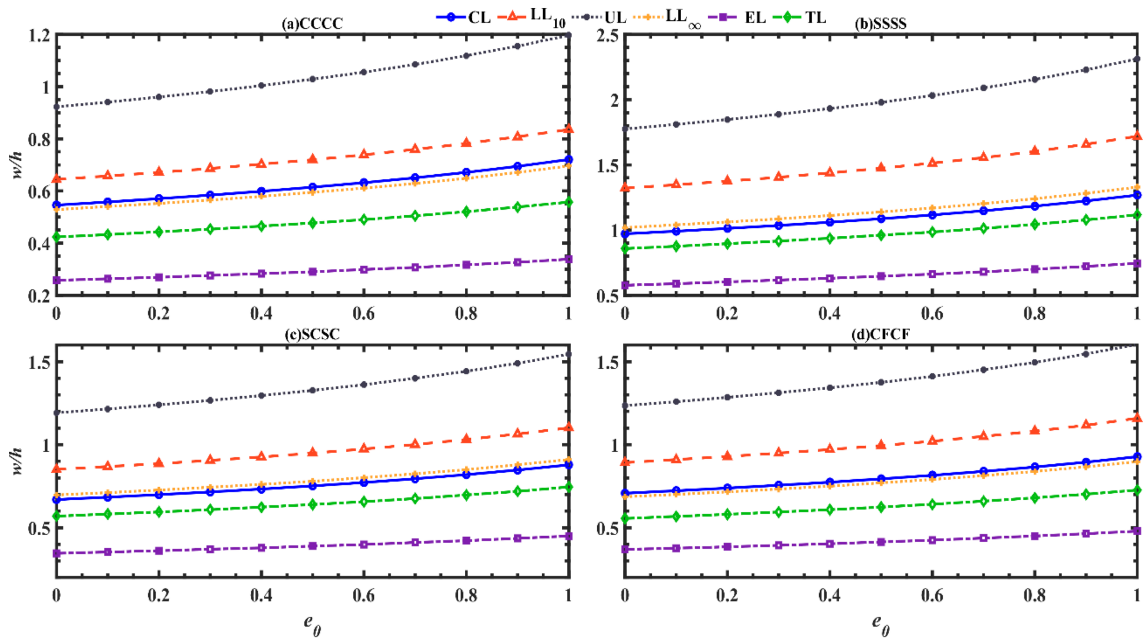

Figure 11. The effect of porosity on the dimensionless central deflection of the sandwich plates.

The effect of the GPLs weight fraction on the dimensionless central deflection curves is illustrated graphically in Figure 12. It is observed that the dimensionless central bending deflection decreases with the enhancement of GPLs weight fraction. The results reveal that the accretion of GPLs can significantly improve the overall stiffness of sandwich plates.

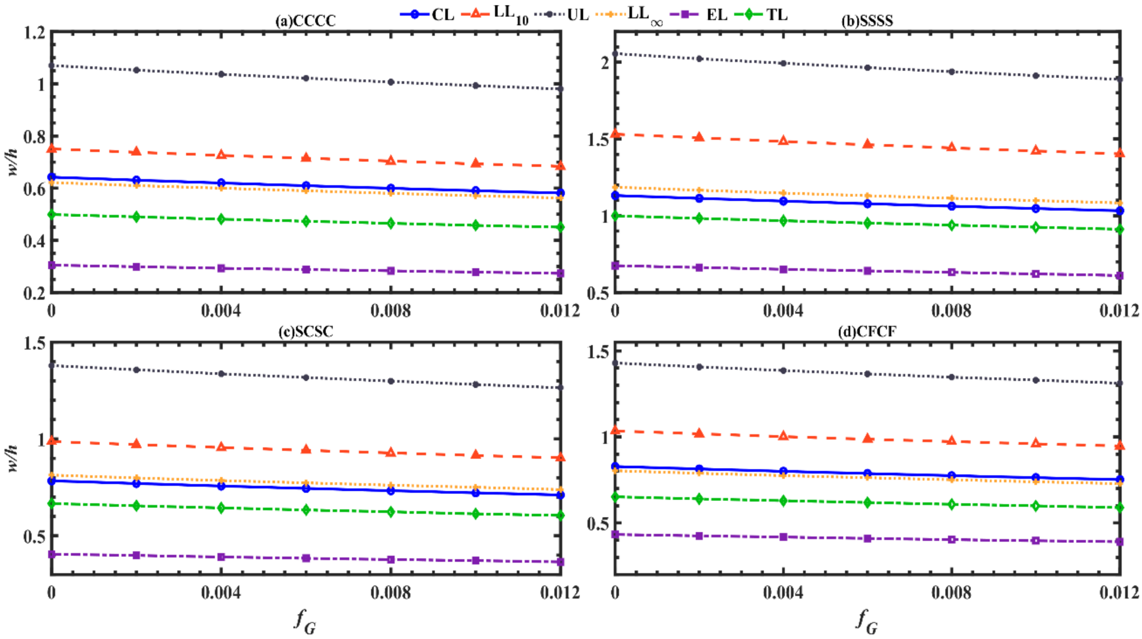

Figure 12. Effect of GPLs weight fraction on the dimensionless central nonlinear bending deflection of the sandwich plates under various boundary conditions.

The effect of GPLs geometry aspect ratio (l_G/w_G) and length-to-thickness ratio (l_G/h_G) on the dimensionless central nonlinear bending deflection of the sandwich plates with length-to-thickness ratio $a/h_t = 5$ and $a/h_t = 10$ has been presented in Figure 13a,b. It can be observed that GPLs with higher aspect ratio and smaller length-to-thickness ratio significantly reduce the stiffness of the sandwich plates. In addition, an increment in the length-to-thickness ratio of the sandwich plates leads to an enhanced dimensionless central nonlinear bending deflection.

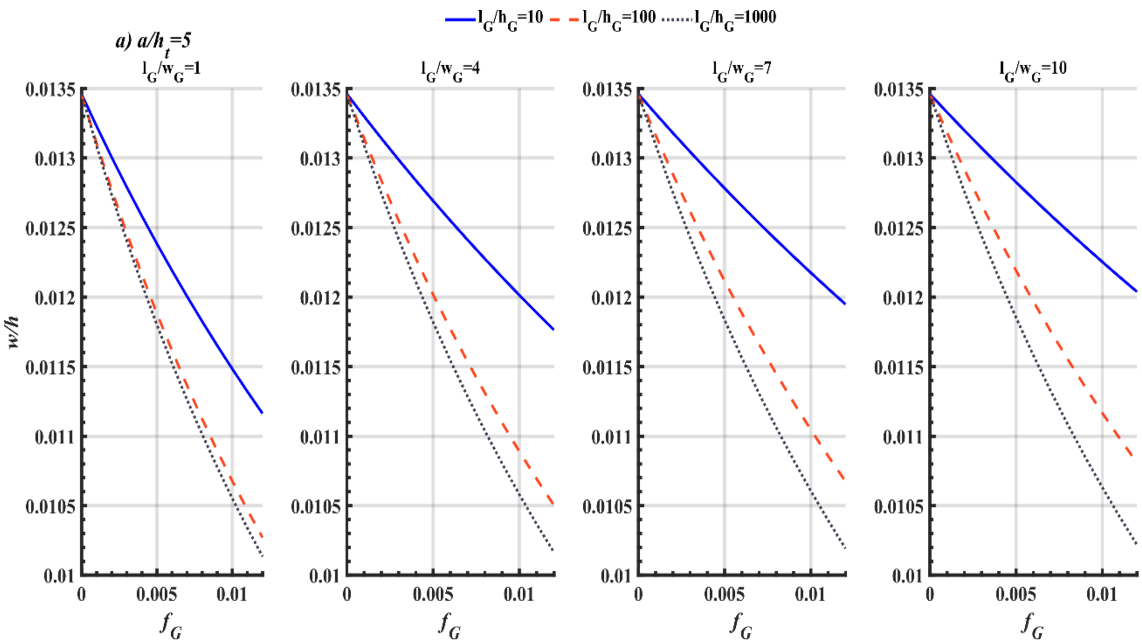

Figure 13. *Cont.*

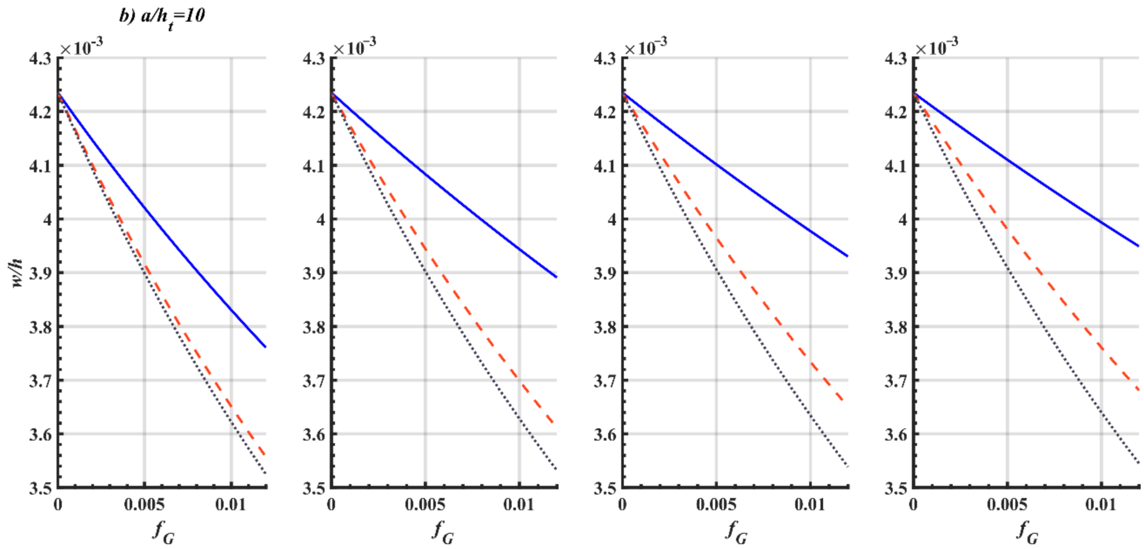

Figure 13. Effect of the GPLs aspect ratio (l_G/w_G) and length-to-thickness ratio (l_G/h_G) on the dimensionless central nonlinear bending deflection of the sandwich plates: (**a**) $a/h_t = 5$, (**b**) $a/h_t = 10$.

The effect of the layer thickness ratio on the nonlinear bending deflection of the porous sandwich plates under different boundary conditions has been shown in Figure 14. As observed, the dimensionless central deflections are higher and lower for the 1-8-1 and 1-0-1 sandwich plates, respectively. The results show that the thicker the core thickness, the smaller the stiffness caused by the pores.

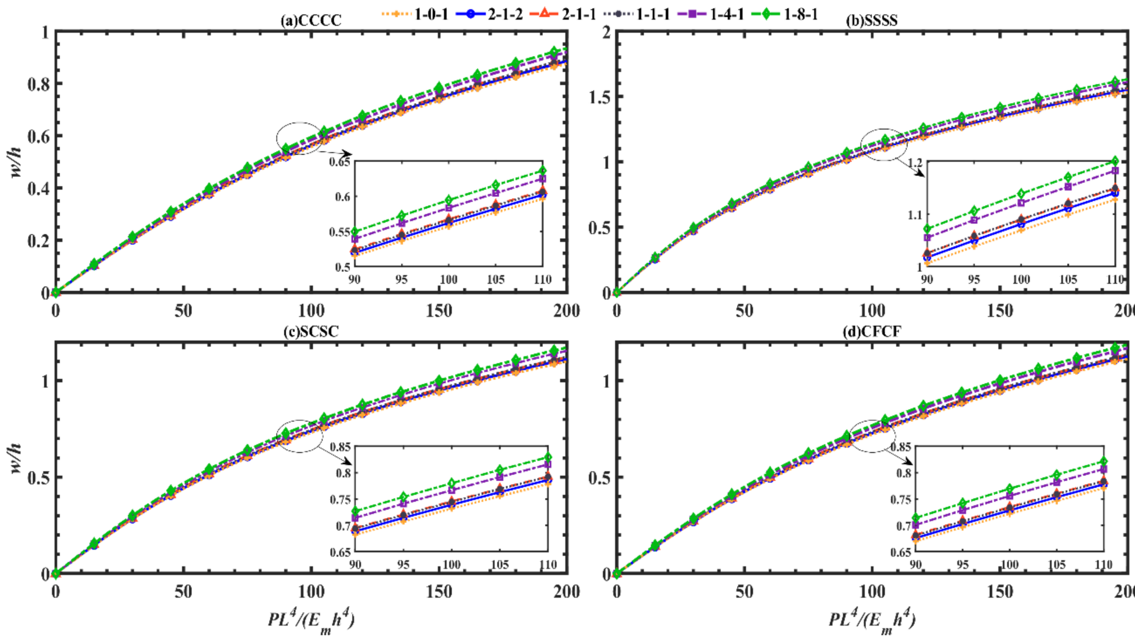

Figure 14. Effect of the layer thickness ratio on the nonlinear bending deflection of the porous sandwich plates under various BCs.

As shown in Figure 15, the nonlinear bending deflection increases with the concentrated load radius. As the radius gradually increases, the load applied to the upper surface becomes larger and closer to the uniform load.

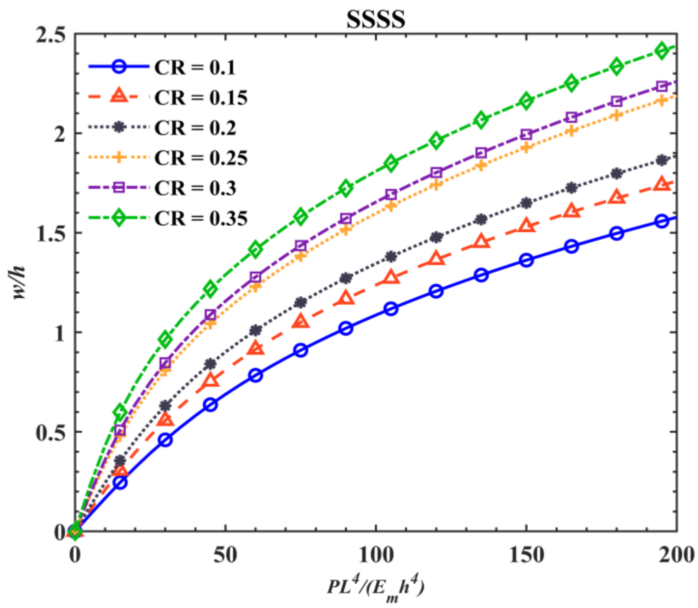

Figure 15. Effect of the concentrated load radius of the porous sandwich plates under the boundary condition SSSS.

6. Conclusions

In this study, nonlinear bending of the sandwich plates with a GNRPC core and two metal skins has been investigated by employing the four-unknown refined theory considering the thickness stretching effects. The mathematical models of the sandwich plates under six load types rest upon the virtual work principle and nonlinear Von Karman strain–displacement relationship. The nonlinear bending deflection has been gained by taking the classical finite element and Newton downhill methods into account. A good agreement is observed between the findings obtained in this study and reported literature. The following conclusions are drawn from the numerical results.

(1) The adopted higher order theory can significantly improve the simulation of the transverse deflection and different stresses in the thickness direction.
(2) All six types of loads have similar mechanical behaviors. According to the dimensionless central deformation caused by them, six load types are sorted with a descending order UL, LL_{10}, CL with CR = 0.1 m, LL_{∞}, TL, EL for CCCC as well as CFCF boundary conditions and UL, LL_{10}, LL_{∞}, CL with CR = 0.1 m, TL, EL for SSSS and SCSC boundary conditions.
(3) The dimensionless central deflection is maximum for the UL and minimum for the EL compared to other examined four different types of load.
(4) Under the same boundary conditions, the dimensionless central nonlinear bending deflection increases with the enhancement of porosity coefficient, GPLs aspect ratio, thickness of porous core layer. However, it shows a reverse trend for the GPLs weight fraction, GPLs length-to-thickness ratio.

Considering the continuous gradient change of the material physical parameters, only one pore distribution and GPLs distribution models in the core layer have been employed in this study. The mechanical behavior of the sandwich plates with core layer is impacted by various pore and GPLs distribution patterns, thus, the sandwich plates with FG GPLs reinforced composite skins will be developed in the future for further insights.

Author Contributions: Conceptualization, X.F., A.W. and S.W.; methodology, X.F., A.W. and P.J.; software, X.F. and P.J.; validation, X.F. and P.J.; formal analysis, X.F., P.J. and A.W.; investigation, A.W. and Y.S.; writing—original draft preparation, X.F., P.J. and A.W.; writing—review and editing, X.F. and A.W.; supervision, A.W.; funding acquisition, A.W. and Y.S. All authors have read and agreed to the published version of the manuscript.

Funding: This work was subsidized by the National Science Foundation of China (Grant Numbers 12272058, 11832002, 11902038). The authors are very grateful to the editor and referees for their criticism. Their valuable comments and suggestions helped to improve this paper.

Institutional Review Board Statement: Not applicable.

Informed Consent Statement: Not applicable.

Data Availability Statement: Not applicable.

Conflicts of Interest: The authors declare no conflict of interest.

Appendix A

$$
\boldsymbol{H} = \begin{bmatrix}
1 & 0 & 0 & 0 & 0 & 0 & 0 & 0 & 0 & 0 & 0 & 0 & 0 & 0 \\
0 & 0 & 1 & 0 & 0 & 0 & 0 & 0 & 0 & 0 & 0 & 0 & 0 & 0 \\
0 & 1 & 0 & 0 & 1 & 0 & 0 & 0 & 0 & 0 & 0 & 0 & 0 & 0 \\
0 & 0 & 0 & 0 & 0 & 1 & 0 & 0 & 0 & 0 & 0 & 0 & 0 & 0 \\
0 & 0 & 0 & 0 & 0 & 0 & 0 & 1 & 0 & 0 & 0 & 0 & 0 & 0 \\
0 & 0 & 0 & 0 & 0 & 0 & 2 & 0 & 0 & 0 & 0 & 0 & 0 & 0 \\
0 & 0 & 0 & 0 & 0 & 0 & 0 & 0 & 0 & 0 & 0 & 1 & 0 & 0 \\
0 & 0 & 0 & 0 & 0 & 0 & 0 & 0 & 0 & 0 & 0 & 0 & 0 & 1 \\
0 & 0 & 0 & 0 & 0 & 0 & 0 & 0 & 0 & 0 & 0 & 0 & 2 & 0 \\
0 & 0 & 0 & 0 & 0 & 0 & 0 & 0 & 0 & 0 & 0 & 0 & 0 & 0 \\
0 & 0 & 0 & 0 & 0 & 0 & 0 & 0 & 0 & 0 & 0 & 0 & 0 & 0 \\
0 & 0 & 0 & 0 & 0 & 0 & 0 & 0 & 0 & 0 & 0 & 0 & 0 & 0 \\
0 & 0 & 0 & 0 & 0 & 0 & 0 & 0 & 0 & 1 & 0 & 0 & 0 & 0 \\
0 & 0 & 0 & 0 & 0 & 0 & 0 & 0 & 0 & 0 & 1 & 0 & 0 & 0 \\
0 & 0 & 0 & 0 & 0 & 0 & 0 & 0 & 0 & 0 & 0 & 0 & 0 & 0 \\
0 & 0 & 0 & 0 & 0 & 0 & 0 & 0 & 0 & 0 & 0 & 0 & 0 & 0 \\
0 & 0 & 0 & 0 & 0 & 0 & 0 & 0 & 0 & 0 & 0 & 0 & 0 & 0 \\
0 & 0 & 0 & 0 & 0 & 0 & 0 & 0 & 1 & 0 & 0 & 0 & 0 & 0 \\
0 & 0 & 0 & 0 & 0 & 0 & 0 & 0 & 0 & 1 & 0 & 0 & 0 & 0 \\
0 & 0 & 0 & 0 & 0 & 0 & 0 & 0 & 0 & 0 & 1 & 0 & 0 & 0
\end{bmatrix}
$$

$$
\boldsymbol{A} = \begin{bmatrix}
0 & 0 & 0 & w_{,x} & 0 & 0 & 0 & 0 & 0 & 0 & 0 & 0 & 0 & 0 \\
0 & 0 & 0 & 0 & w_{,y} & 0 & 0 & 0 & 0 & 0 & 0 & 0 & 0 & 0 \\
0 & 0 & 0 & w_{,y} & w_{,x} & 0 & 0 & 0 & 0 & 0 & 0 & 0 & 0 & 0 \\
0 & 0 & 0 & 0 & 0 & 0 & 0 & 0 & 0 & 0 & 0 & 0 & 0 & 0 \\
0 & 0 & 0 & 0 & 0 & 0 & 0 & 0 & 0 & 0 & 0 & 0 & 0 & 0 \\
0 & 0 & 0 & 0 & 0 & 0 & 0 & 0 & 0 & 0 & 0 & 0 & 0 & 0 \\
0 & 0 & 0 & 0 & 0 & 0 & 0 & 0 & 0 & 0 & 0 & 0 & 0 & 0 \\
0 & 0 & 0 & 0 & 0 & 0 & 0 & 0 & 0 & 0 & 0 & 0 & 0 & 0 \\
0 & 0 & 0 & 0 & 0 & 0 & 0 & 0 & 0 & 0 & 0 & 0 & 0 & 0 \\
0 & 0 & 0 & \varphi_{,x} & 0 & 0 & 0 & 0 & 0 & w_{,x} & 0 & 0 & 0 & 0 \\
0 & 0 & 0 & 0 & \varphi_{,y} & 0 & 0 & 0 & 0 & 0 & w_{,y} & 0 & 0 & 0 \\
0 & 0 & 0 & \varphi_{,y} & \varphi_{,x} & 0 & 0 & 0 & 0 & w_{,y} & w_{,x} & 0 & 0 & 0 \\
0 & 0 & 0 & 0 & 0 & 0 & 0 & 0 & 0 & 0 & 0 & 0 & 0 & 0 \\
0 & 0 & 0 & 0 & 0 & 0 & 0 & 0 & 0 & 0 & 0 & 0 & 0 & 0 \\
0 & 0 & 0 & 0 & 0 & 0 & 0 & 0 & 0 & \varphi_{,x} & 0 & 0 & 0 & 0 \\
0 & 0 & 0 & 0 & 0 & 0 & 0 & 0 & 0 & 0 & \varphi_{,y} & 0 & 0 & 0 \\
0 & 0 & 0 & 0 & 0 & 0 & 0 & 0 & 0 & \varphi_{,y} & \varphi_{,x} & 0 & 0 & 0 \\
0 & 0 & 0 & 0 & 0 & 0 & 0 & 0 & 0 & 0 & 0 & 0 & 0 & 0 \\
0 & 0 & 0 & 0 & 0 & 0 & 0 & 0 & 0 & 0 & 0 & 0 & 0 & 0 \\
0 & 0 & 0 & 0 & 0 & 0 & 0 & 0 & 0 & 0 & 0 & 0 & 0 & 0
\end{bmatrix}
$$

References

1. Lefebvre, L.P.; Banhart, J.; Dunand, D.C. Porous metals and metallic foams: Current status and recent developments. *Adv. Eng. Mater.* **2008**, *10*, 775–787. [CrossRef]
2. Wang, Y.Q.; Ye, C.; Zu, J.W. Nonlinear vibration of metal foam cylindrical shells re-inforced with graphene platelets. *Aerosp. Sci. Technol.* **2019**, *85*, 359–370. [CrossRef]
3. Yaghoobi, H.; Taheri, F. Analytical solution and statistical analysis of buckling capacity of sand- wich plates with uniform and non-uniform porous core reinforced with graphene nanoplatelets. *Compos. Struct.* **2020**, *252*, 112700. [CrossRef]
4. Rafiee, M.A.; Rafiee, J.; Wang, Z.; Song, H.H.; Yu, Z.Z.; Koratkar, N. Enhanced mechanical properties of nanocomposites at low graphene content. *ACS Nano* **2009**, *3*, 3884–3890. [CrossRef]
5. Yang, J.; Wu, H.L.; Kitipornchai, S. Buckling and postbuckling of functionally graded multilayer graphene platelet-reinforced composite beams. *Compos. Struct.* **2017**, *161*, 111–118. [CrossRef]
6. Guo, H.L.; Cao, S.Q.; Yang, T.Z.; Chen, Y.S. Vibration of laminated composite quadrilateral plates reinforced with graphene nanoplatelets using the element-free IMLS-Ritz method. *Int. J. Mech. Sci.* **2018**, *142–143*, 610–621. [CrossRef]
7. Mao, J.J.; Zhang, W. Linear and nonlinear free and forced vibrations of graphene reinforced piezoelectric composite plate under external voltage excitation. *Compos. Struct.* **2018**, *203*, 551–565. [CrossRef]
8. Wang, A.W.; Chen, H.Y.; Hao, Y.X.; Zhang, W. Vibration and bending behavior of functionally graded nanocomposite doubly-curved shallow shells reinforced by graphene nanoplatelets. *Results Phys.* **2018**, *9*, 550–559. [CrossRef]
9. Fu, T.; Chen, Z.B.; Yu, H.Y.; Wang, Z.L.; Liu, X.X. An analytical study of sound transmission through corrugated core FGM sandwich plates with porous material. *Compos. Part B Eng.* **2018**, *151*, 161–172. [CrossRef]
10. Zeng, S.; Wang, B.; Wang, K.F. Nonlinear vibration of piezoelcetric sandwich nanoplates with functionally graded porous core with consideration of flexoelectric effect. *Compos. Struct.* **2019**, *207*, 340–351. [CrossRef]
11. Yu, Y.; Shen, H.S.; Wang, H.; Hui, D. Postbuckling of sandwich plates with graphene-reinforced composite face sheets in thermal environments. *Compos. Part B Eng.* **2018**, *135*, 72–83. [CrossRef]
12. Allam, M.N.M.; Radwan, A.F.; Sobhy, M. Hygrothermal deformation of spinning FG graphene sandwich cylindrical shells having an auxetic core. *Eng. Struct.* **2022**, *251*, 11343. [CrossRef]
13. Arefi, M.; Najafitabar, F. Buckling and free vibration analyses of a sandwich beam made of a soft core with FG-GNPs reinforced composite face-sheets using Ritz Method. *Thin-Walled Struct.* **2021**, *158*, 107200. [CrossRef]
14. Nguyen, N.V.; Nguyen, X.H.; Nguyen, T.N.; Kang, J.; Lee, J. A comprehensive analysis of auxetic honeycomb sandwich plates with graphene nanoplatelets reinforcement. *Compos. Struct.* **2021**, *259*, 113213. [CrossRef]
15. Aydogdu, M. A new shear deformation theory for laminated composite plates. *Compos. Struct.* **2009**, *89*, 94–101. [CrossRef]
16. Li, C.; Shen, H.S.; Yang, J.; Wang, H. Low-velocity impact response of sandwich plates with GRC face sheets and FG auxetic 3D lattice cores. *Eng. Anal. Bound. Elem.* **2021**, *132*, 335–344. [CrossRef]
17. Yadav, A.; Amabili, M.; Panda, S.K.; Dey, T. Nonlinear analysis of cylindrical sandwich shells with porous core and CNT reinforced face-sheets by higher-order thickness and shear deformation theory. *Eur. J. Mech. A Solids* **2021**, *90*, 104366. [CrossRef]
18. Karimiasl, M.; Alibeigloo, A. Nonlinear free and forced vibration analysis of sandwich cylindrical panel with auxetic core and GPLRC facing sheets in hygrothermal environment. *Thin-Walled Struct.* **2022**, *175*, 109164. [CrossRef]
19. Safaei, B.; Moradi-Dastjerdi, R.; Behdinan, K.; Chu, F. Critical buckling temperature and force in porous sandwich plates with CNT-reinforced nanocomposite layers. *Aerosp. Sci. Technol.* **2019**, *91*, 175–185. [CrossRef]
20. Tao, C.; Dai, T. Isogeometric analysis for postbuckling of sandwich cylindrical shell panels with graphene platelet reinforced functionally graded porous core. *Compos. Struct.* **2021**, *260*, 113258. [CrossRef]
21. Chen, X.H.; Shen, H.S. Thermo-mechanical postbuckling analysis of sandwich cylindrical panels with functionally graded auxetic GRMMC core supported by elastic foundations. *Ocean. Eng.* **2022**, *247*, 110661. [CrossRef]
22. Chen, X.H.; Shen, H.S.; Xiang, Y. Thermo-mechanical postbuckling analysis of sandwich cylindrical shells with functionally graded auxetic GRMMC core surrounded by an elastic medium. *Thin-Walled Struct.* **2022**, *171*, 108755. [CrossRef]
23. Twinkle, C.M.; Pitchaimani, J. Static stability and vibration behavior of graphene platelets reinforced porous sandwich cylindrical panel under non-uniform edge loads using semi-analytical approach. *Compos. Struct.* **2022**, *280*, 114837. [CrossRef]
24. Li, Q.Y.; Wu, D.; Chen, X.J.; Liu, L.; Yu, Y.G.; Gao, W. Nonlinear vibration and dynamic buckling analyses of sandwich functionally graded porous plate with graphene platelet reinforcement resting on Winkler–Pasternak elastic foundation. *Int. J. Mech. Sci.* **2018**, *148*, 596–610. [CrossRef]
25. Zhu, C.S.; Fang, X.Q.; Liu, J.X.; Nie, G.Q. Smart control of large amplitude vibration of porous piezoelectric conical sandwich panels resting on nonlinear elastic foundation. *Compos. Struct.* **2020**, *246*, 112384. [CrossRef]
26. Polit, O.; Anant, C.; Anirudh, B.; Ganapathi, M. Functionally graded graphene reinforced porous nanocomposite curved beams: Bending and elastic stability using a higher-order model with thickness stretch effect. *Compos. Part B Eng.* **2019**, *166*, 310–327. [CrossRef]
27. Zenkour, A. A simple four-unknown refined theory for bending analysis of functionally graded plates. *Appl. Math. Model.* **2013**, *37*, 9041–9051. [CrossRef]
28. Ferreira, A.J.M. *Matlab Codes for Finite Element Analysis: Solids and Structures*; Springer: Dordrecht, The Netherlands, 2009.
29. Walter, G. *Numerical Analysis*, 2nd ed.; Springer: New York, NY, USA, 2012.

30. Wang, A.W.; Chen, H.Y.; Zhang, W. Nonlinear transient response of doubly curved shallow shells reinforced with graphene nanoplatelets subjected to blast loads considering thermal effects. *Compos. Struct.* **2019**, *225*, 111063. [CrossRef]
31. Choe, J.C.; Huang, Q.; Yang, J.; Hu, H. An efficient approach to investigate the post-buckling behaviors of sandwich structures. *Compos. Struct.* **2018**, *201*, 377–388. [CrossRef]
32. Yu, K.; Hu, H.; Tang, H.Y.; Giunta, G.; Potier-Ferry, M.; Belouettar, S. A novel two-dimensional finite element to study the instability phenomena of sandwich plates. *Comput. Methods Appl. Mech. Eng.* **2015**, *283*, 1117–1137. [CrossRef]
33. Song, M.T.; Yang, J.; Kitipornchai, S. Bending and buckling analyses of functionally graded polymer composite plates reinforced with graphene nanoplatelets. *Compos. Part B Eng.* **2018**, *134*, 106–113. [CrossRef]
34. Nguye-Xuan, H.; Tran, L.V.; Nguyen-Thoi, T.; Vu-Do, H.C. Analysis of functionally graded plates using an edge-based smoothed finite element method. *Compos. Struct.* **2011**, *93*, 3019–3039. [CrossRef]
35. Gilhooley, D.F.; Batra, R.C.; Xiao, J.R.; McCarthy, M.A.; Gillespie, J.W. Analysis of thick functionally graded plates by using higher-order shear and normal deformable plate theory and MLPG method with radial basis functions. *Compos. Struct.* **2007**, *80*, 539–552. [CrossRef]
36. Lee, Y.Y.; Zhao, X.; Liew, K.M. Thermoelastic analysis of functionally graded plates using the element-free kp-Ritz method. *Smart Mater. Struct.* **2009**, *18*, 035007. [CrossRef]